ARTICLE   OPEN

Check for updates

Sensitivity of the electronic and magnetic structures of cuprate superconductors to density functional approximations

Kanun Pokharel[1✉], Christopher Lane[2,3✉], James W. Furness [1], Ruiqi Zhang [1], Jinliang Ning[1], Bernardo Barbiellini [4,5], Robert S. Markiewicz[5], Yubo Zhang[1], Arun Bansil[5✉] and Jianwei Sun [5✉]

We discuss the crystal, electronic, and magnetic structures of $La_{2-x}Sr_xCuO_4$ (LSCO) for $x = 0.0$ and $x = 0.25$ employing 13 density functional approximations, representing the local, semi-local, and hybrid exchange-correlation approximations within the Perdew–Schmidt hierarchy. The meta-generalized gradient approximation (meta-GGA) class of functionals is found to perform well in capturing the key properties of LSCO, a prototypical high-temperature cuprate superconductor. In contrast, the localspin-density approximation, GGA, and the hybrid density functional fail to capture the metal-insulator transition under doping.

INTRODUCTION

Ever since the discovery of cuprate superconductivity in 1986 by Bednorz and Müller[1], the anomalous behavior of the pristine, as well as the doped cuprate, has eluded theoretical explanation and still remains an unsolved problem in condensed matter physics. La_2CuO_4 (LCO), in particular, has been a significant challenge to describe within a coherent theoretical framework. The Hohenberg–Kohn–Sham density functional theory (DFT)[2,3] with some classes of popular exchange-correlation (XC) approximations fails spectacularly to capture the insulating antiferromagnetic ground state of LCO, let alone the metal insulator transition (MIT) under doping[4]. Specifically, the local spin-density approximation (LSDA) XC functional incorrectly predicts the parent compound to be a metal, yielding a vastly underestimated value for the copper magnetic moment of $0.1\mu_B$[5,6] compared to the experimental value of $0.60 \pm 0.05\mu_B$[7]. The Perdew-Burke-Ernzerhof (PBE) generalized gradient approximation (GGA)[8] still predicts LCO to be a metal with a slightly improved magnetic moment of $0.2\mu_B$[9]. The Becke-3–Lee–Yang–Parr (B3LYP)[10–13] hybrid functional correctly explains the AFM ground state in LCO but fails to capture the MIT upon doping[14]. These failures have led to the (incorrect) belief that DFT is fundamentally incapable of capturing the physics of the cuprates and other correlated materials. Therefore, "beyond DFT" methodologies, such as the quantum Monte Carlo methods[15], DFT+U[16,17], and dynamical mean-field theory (DMFT)[18–20] have been introduced to handle strong electron correlation effects. These approaches have been useful for understanding the physics of the cuprates, although they typically introduce ad hoc parameters, such as the Hubbard U, to tune the correlation strength, which limits their predictive power.

Recent progress in constructing advanced density functional approximations (DFA) provides a viable new pathway for addressing the electronic structures of correlated materials. In particular, the strongly-constrained and appropriately-normed (SCAN) meta-GGA[21], which obeys all 17 known constraints applicable to a meta-

GGA functional, has been shown to accurately predict many key properties of the pristine and doped La_2CuO_4 and $YBa_2Cu_3O_6$[22–24]. In LCO, SCAN correctly captures the size of the optical bandgap, the magnitude and the orientation of the copper magnetic moment, and the magnetic form factor in comparison with the corresponding experimental results[23]. In near-optimally doped $YBa_2Cu_3O_7$, 26 competing uniform and stripe phases are identified[24]. In this case, the treatment of charge, spin, and lattice degrees of freedom on the same footing is crucial in stabilizing the stripe phases without invoking any free parameters. Furthermore, SCAN has been applied to the Sr_2IrO_4 parent compound yielding the subtle balance between electron correlations and strong spin-orbit coupling in excellent agreement with experiment[25].

SCAN's success in the copper and iridium oxides is a significant achievement for the DFT and suggests capability for treating a wider class of correlated materials. SCAN, however, is well-known to yield overly large saturation magnetization in elemental metals (e.g., Fe and Ni)[26–28] and has the problem of numerical instabilities[29–32], which may limit its applicability. A number of natural questions, therefore, arise: Is SCAN a unique XC density function that is able to correctly capture a variety of properties of the cuprates or do other meta-GGAs perform similarly well? How do hybrid XC functionals perform in comparison? Answers to these questions are important for benchmarking the performance of SCAN and related DFAs and for opening a pathway to their more extensive use.

With this motivation, this paper compares the accuracy of 13 DFAs. In particular, we assess the efficacy of LSDA[33,34], PBE[8], SCAN[21], SCAN-L[35], rSCAN[31], r²SCAN[32], r²SCAN-L[36], TPSS[37], revTPSS[38], MS0[39], MS2[40], M06L[41], and HSE06[42–45] with respect to their predictions for crystal, electronic, and magnetic structures of the pristine and doped prototypical high-temperature superconductors $La_{2-x}Sr_xCuO_4$. Various XC density functionals were employed to span the levels of the Perdew–Schmidt hierarchy[46], allowing us to evaluate the performance of each functional class for the description of correlated condensed matter systems.

[1]Department of Physics and Engineering Physics, Tulane University, New Orleans, LA 70118, USA. [2]Theoretical Division, Los Alamos National Laboratory, Los Alamos, NM 87545, USA. [3]Center for Integrated Nanotechnologies, Los Alamos National Laboratory, Los Alamos, NM 87545, USA. [4]Department of Physics, School of Engineering Science, LUT University, FI-53851 Lappeenranta, Finland. [5]Physics Department, Northeastern University, Boston, MA 02115, USA. ✉email: kpokhare@tulane.edu; laneca@lanl.gov; ar.bansil@neu.edu; jsun@tulane.edu

2

RESULTS AND DISCUSSION

Methodology

The theoretical foundation of DFT was laid by Hohenberg and Kohn[2] when they considered the *electron density* rather than the wave function as the fundamental object for addressing the many-body problem. This concept was later extended by Kohn and Sham (KS) by replacing the complicated many-electron problem with an auxiliary non-interacting system that leads to the one-electron Schrödinger like equations[3], providing a practical approach to solve for the ground-state electron density and ground-state energy of the many-body system. The beauty of the KS approach is that it explicitly separates the non-interacting kinetic energy and the long-range Hartree energy, which describes the classical electrostatic repulsion between electrons, from the remaining exchange-correlation energy. An exact solution for the ground-state total energy and electron density is then obtained, in principle, although in practice, the XC energy must be approximated.

The total energy of the many-body electron system, within the Kohn–Sham DFT framework can be written as:

$$E = T_s + E_{ext} + E_H + E_{xc}, \qquad (1)$$

where T_s is the non-interacting kinetic energy, E_{ext} is the external potential energy, E_H is the Hartree energy, and E_{xc} contains the remaining energy contributed by the many-body XC effects. The first three terms in Eq. (1) can be obtained exactly while the last term has to be approximated. Various approximations for E_{xc} can be arranged on the rungs of the Perdew–Schmidt hierarchy[46]. The lowest rung of the hierarchy is LSDA that is based on local electron densities n_σ. On the next rung, the GGA class adds density gradients ∇n_σ to LSDA. This is followed by meta-GGAs that come in two flavors, adding either the non-interacting kinetic energy density τ_σ or a Laplacian dependence $\nabla^2 n_\sigma$ or both in comparison with GGAs. Here σ denotes the two spin channels. The XC energy for meta-GGAs is defined as

$$E_{xc}^{MGGA}[n_\uparrow, n_\downarrow] = \int d^3\mathbf{r}\, n(\mathbf{r})\varepsilon_x^{unif}(n)F_{xc}(n_\uparrow, n_\downarrow, \nabla n_\uparrow, \nabla n_\downarrow, \nabla^2 n_\uparrow, \nabla^2 n_\downarrow, \tau_\uparrow, \tau_\downarrow). \qquad (2)$$

where $\varepsilon_x^{unif}(n)$ is the exchange energy per electron for the uniform electron gas and F_{xc} is an enhancement factor.

By including τ, the meta-GGA functional becomes more flexible and allows for satisfying a greater number of exact constraints compared to GGAs. Furthermore, by defining a dimensionless variable $\alpha = \frac{\tau - \tau^w}{\tau^{unif}}$, where $\tau^{unif} = (3/10)(3\pi^2)^{2/3} n^{5/3}$ is the kinetic energy density of the uniform electron gas and $\tau^w = |\nabla n|^2/8n$ is the von Weizsäcker kinetic energy density, a meta-GGA can recognize slowly varying densities, single-orbital systems, and non-covalent bonds between two closed shells[21,47,48]. Moreover, since τ is determined from the set of KS orbitals, meta-GGAs with explicit τ dependence are intrinsically non-local in nature. DFAs in this class include SCAN, Regularized SCAN (rSCAN)[31], regularized-restored SCAN (r2SCAN)[32,49], Tao–Perdew–Staroverov–Scuseria (TPSS)[37], revised-TPSS (revTPSS)[38], meta-GGA made simple 0 (MS0)[39], meta-GGA made simple 2 (MS2)[40], and the Minnesota functional (M06L)[41].

Trickey et al. recently substituted functions of $\nabla^2 n(\mathbf{r})$ for $\tau(\mathbf{r})$ in meta-GGA XC functionals, leading to SCAN-L[35,50] and r2SCAN-L[36] XC density functionals, among others, which yield similar (but not identical) performance to the original orbital dependent versions. The last class considered in this article are the hybrid functionals, which were originally designed to combine a semi-local DFA with the exact exchange of the Hartree–Fock single determinant to improve predictions of molecular thermochemical properties. The idea is that since the semi-local DFAs typically overbind while Hartree–Fock underbinds, their combination would presumably capture the correct balance between the two limits. The XC energy for the screened hybrid functional of Heyd, Scuseria, and Ernzerhof (HSE) is given by

$$\begin{aligned}E_{xc}^{HSE} = &\, aE_x^{HF,SR}(\omega) + (1-a)E_x^{PBE,SR}(\omega) \\ &+ E_x^{PBE,LR}(\omega) + E_c^{PBE},\end{aligned} \qquad (3)$$

where a is the exact exchange admixing parameter whose typical value is $1/4$[51]. Here, the screening parameter ω defines the separation range, $E_x^{HF,SR}(\omega)$ the short-range HF exact exchange, and $E_x^{PBE,SR}(\omega)$ and $E_x^{PBE,LR}(\omega)$ the short and long-range components, respectively, of the PBE exchange functional. The admixing parameter value of $a = 1/4$ has been justified through a consideration of molecular thermochemical properties[52].

Ground-state crystal structure

The phase diagram of the cuprates displays a complex intertwining of magnetic and charge-ordered states that evolve with doping to reveal a superconducting dome. Interestingly, structural phase transitions associated with various octahedral tilt modes[53,54] mainly follow the electronic phase boundaries.[55] At high temperatures LCO is found to be tetragonal (HTT) with all CuO_6 octahedra aligned axially. A phase transition occurs upon lowering the temperature resulting in a low-temperature orthorhombic (LTO) phase where the octahedra are tilted along the (110) zone diagonal. An additional low-temperature tetragonal (LTT) phase arises upon substituting La with Ba or Nd, where the octahedral tilts are aligned along the (100) and (010) directions in alternating CuO_2 layers. Therefore, in order to properly disentangle the connection between the electronic and the physical properties of the cuprates, it is imperative to capture the correct ground-state crystal structure. To calculate the total energies of various crystalline phases, we consider the $\sqrt{2} \times \sqrt{2}$ supercell of the body-centered-tetragonal I4/mmm primitive unit cell to accommodate both the octahedral tilts and the (π, π) AFM order within the CuO_2 planes. We treat the doping within a relatively simple "δ- doping" scheme in which one La atom in the supercell is replaced by a Sr atom to yield an average hole doping of 25%[22]. This approach has been recently used for doping LSCO via molecular beam epitaxy techniques[56]. Figure 1a shows the crystal structures of LCO and LSCO in the LTO phase where the CuO_6 octahedra have been shaded blue and orange to represent the AFM order. The Sr doping site is also indicated.

Figure 2a and d present energy differences between the AFM and NM phases for the pristine and doped $La_{2-x}Sr_xCuO_4$ in each crystal structure for the DFAs considered. Firstly, we note that LSDA does not stabilize an AFM order over the Cu sites, whereas in PBE the AFM phase is marginally more stable, consistent with the previous studies[22]. All meta-GGAs find the AFM phase to be the ground state, with an energy separation of -0.2 to -0.9 eV between the AFM and NM states in the pristine structure, whereas in the doped case the energy difference is smaller by a factor of two. These trends are consistent across the various crystal structures.

Figure 2b, c, e, f presents energy differences between the HTT, LTT, and LTO crystal structures for pristine and doped $La_{2-x}Sr_xCuO_4$ for various density functional approximations. In all cases, the HTT phase lies at much higher energy compared to the LTO and LTT phases. Difference between the LTO and LTT appears more delicate. For the undoped case, only SCAN correctly predicts LTO to be the ground state, while LSDA, rSCAN, r2SCAN, and r2SCAN-L find LTO and LTT to be nearly degenerate with an energy difference of less than 1 meV. In the doped case, all XC functionals correctly predict the ground state to be LTT[57], while SCAN and rSCAN yield a marginal energy difference between LTT and LTO. Note that near 12% doping, the LTO and LTT phases are found experimentally to be virtually degenerate[22].

Figure 3 shows the equilibrium lattice constants for LCO in the HTT, LTT, and LTO phases. The LSDA and PBE values were taken
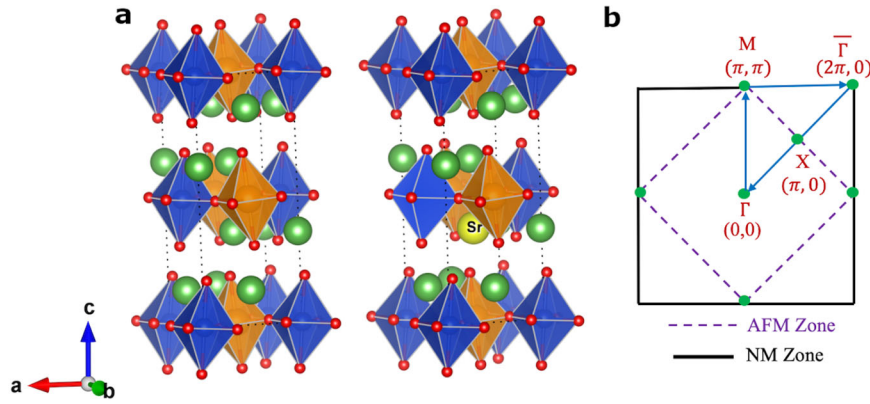
Fig. 1 LTO crystal structure and brillouine zone considered for the calculation. a Theoretically predicted crystal structure of $La_{2-x}Sr_xCuO_4$ in the LTO phase for $x = 0.0$ and 0.25. Copper, oxygen, lanthanum, and strontium atoms are represented by blue, red, green, and yellow spheres, respectively. Octahedral faces are shaded in blue (orange) to denote spin-up (down). Black dotted lines mark the unit cell. **b** A schematic of the non-magnetic (NM) and anti-ferromagnetic (AFM) Brillouin zone, where the path followed in the electronic dispersions in Fig. 6 is marked.
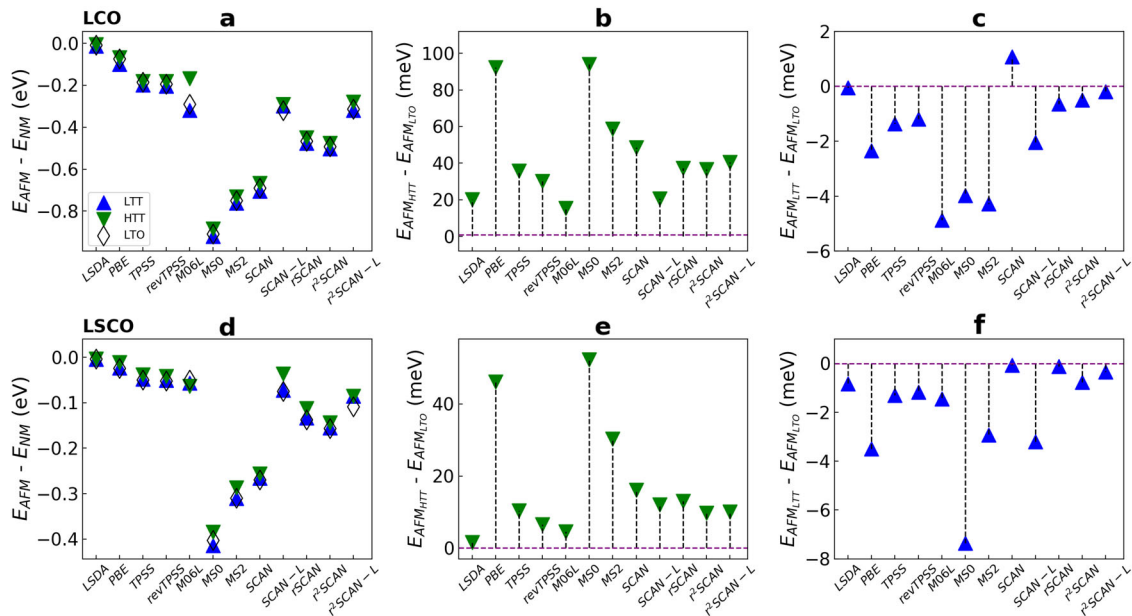
Fig. 2 Various energy calculations obtained for all three phases using different DFAs. a Energy differences between the G-AFM and NM phases for the HTT (green upside-down triangle), LTO (white diamond), and LTT (blue triangle) structures for various XC density functionals. **b, c** Relative energies per formula unit for AFM in pristine LCO between LTO and HTT (**b**) and LTO and LTT (**c**). **d–f** Same as **a–c** except that these panels refer to LSCO instead of LCO.

from ref. [22] and experimental values from refs. [58–60]. The LSDA is seen to underestimate the lattice constant for all crystal structures. PBE, on the other hand, underbinds the atoms and yields an exaggerated orthorhombicity in the LTO phase, similar to the super-tetragonality spuriously predicted by PBE for ferroelectric materials[61]. TPSS, revTPSS, MS0, MS2, SCAN, SCAN-L, rSCAN, r^2SCAN and r^2SCAN-L correct PBE by reducing the b lattice constant in line with the experimental values in LTO and LTT.

Curiously, all XC density functionals underestimate the lattice parameters in the HTT phase, except for PBE and M06L. The empirical M06L XC functional predicts lattice constants with greater accuracy than other XC functionals in all cases. Note that HTT is a high-temperature phase and therefore the experimental lattice constant should, in principle, be corrected for finite-temperature effects for comparison with DFT results. Figure 4 considers the octahedral tilt angles. Here, M06L underestimates the tilt angle, while all other XC functionals overestimate it within a few degrees. We note, however, that the experimental tilt angles should be regarded as average

values because the CuO_6 octahedra are not rigid objects: these octahedra couple to various phonon modes and deform dynamically. Molecular dynamics or phonon calculations will be needed to capture the octahedral tilts more accurately.

Lattice constants and octahedral tilts are not included for r^2SCAN-L in Figs. 3 and 4 because we found a non-zero stress tensor at the energy-minimized equilibrium volume in this case. This suggests an error in the stress tensor implementation of r^2SCAN-L, see Supplementary Discussion 1 in the Supplementary Materials for more details. The experimental structures were therefore used for the electronic and magnetic properties calculations using r^2SCAN-L. The experimental structures were also used for HSE06-based calculations as the computational cost for hybrid XC functionals is much greater than the meta-GGAs.

Notably, within the "SCAN family" of XC density functionals (SCAN, SCAN-L, rSCAN, and r^2SCAN) all members show similar performance for lattice constants and tilt angles (Figs. 3 and 4). The potential speedup of running r^2SCAN-L in a density-only KS scheme and the
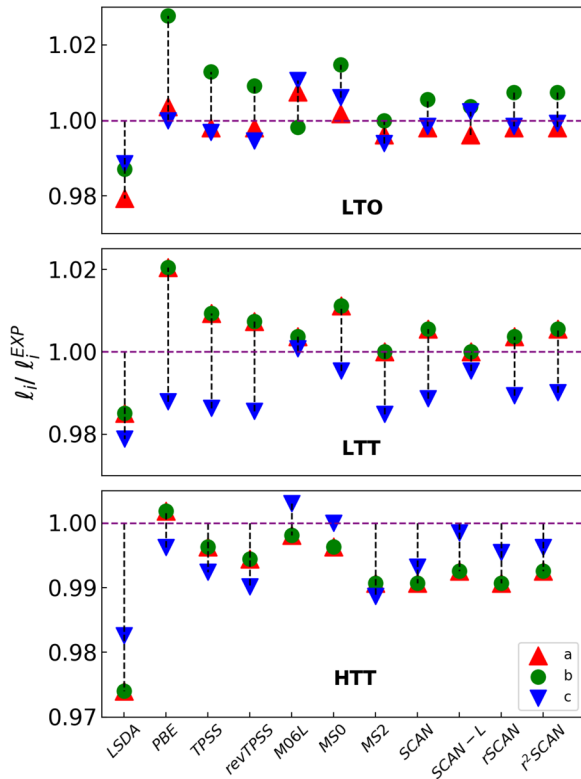
Fig. 3 Comparison of the theoretically obtained and experimental lattice constants a, b, c for the HTT, LTT, and LTO crystal structures using various density functional approximations for La$_2$CuO$_4$. The lattice constant values are divided by corresponding experimental values.
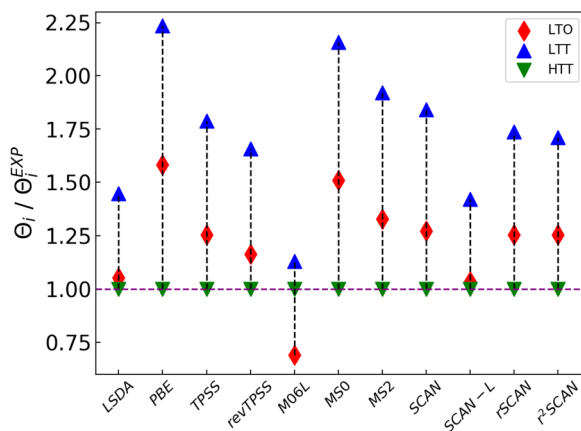

Fig. 4 Theoretically predicted values of octahedra tilt angle using various density functional approximations for LCO. The LSDA and PBE values are taken from ref. [22] The octahedra tilt values for LTO, LTT, and HTT are divided by corresponding experimental values.

improved numerical performance inherited from r^{2}SCAN suggest that r^{2}SCAN-L could be used to optimize geometry followed by a single point SCAN or r^{2}SCAN calculation for obtaining electronic properties. This approach may also present an advantage of minimizing the numerical challenges associated with SCAN. A similar scheme was suggested in ref. [62] in the context of spin-crossover prediction.

Electronic and magnetic structures

Figure 5 compares the theoretically predicted electronic bandgaps and copper magnetic moments obtained from various XC
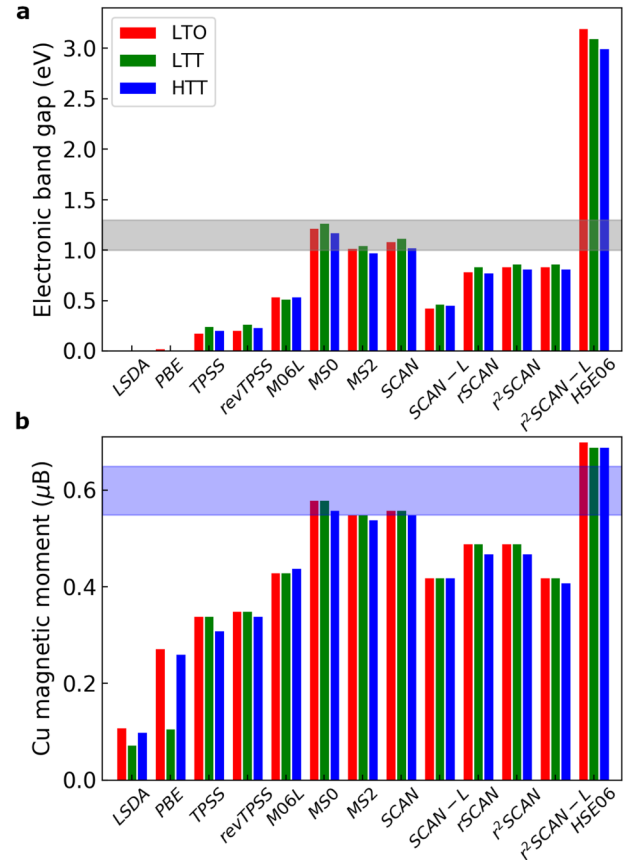
Fig. 5 Band gap and magnetic moment values from various DFAs. Theoretical predicted values of **a** electronic bandgap and **b** copper magnetic moment for all three phases of pristine LCO obtained within various density functional approximations. The gray shaded region in **a** gives the spread in the reported experimental values for the leading edge gap[63–65]. In **b**, the blue shaded region represents the experimental value of magnetic moment[7]. The LSDA and PBE values are taken from ref. [22].

functionals for the three crystalline phases of LCO. The range of experimentally observed bandgaps[63–65], and median copper magnetic moments[7] are marked by the gray and blue shaded regions, respectively. LSDA and PBE greatly underestimate the bandgaps and magnetic moments because they fail to stabilize the AFM order. A large variation is seen in the results of the meta-GGAs. TPSS and revTPSS both underestimate the bandgaps and magnetic moments. MS0, MS2, and SCAN yield values that lie within the experimental ranges. Other meta-GGAs predict reduced bandgaps and magnetic moments that are below experimental values. M06L underestimates both the moment and the bandgap value, possibly due to the bias towards molecular systems which is encoded in its empirical construction. M06L yields ferrimagnetic order and, therefore, the average of the magnetic moment is given in Fig. 5. Finally, the hybrid functional (HSE06) overestimates bandgaps, predicting a value of around 3 eV, and it also overestimates magnetic moments.

Ando[66] has stressed that one should estimate the bandgap not from the lowest energy absorption peak, but from the leading edge gap in the optical spectra[63]. The leading edge gives the minimum energy needed by an electron to be elevated from the valence to the conduction band, in good agreement with the transport gap in the cuprates. In contrast, the energy of the absorption peak in the optical spectrum depends on finer details of the electronic structure such as the presence of flat bands or Van Hove singularities. The theoretically predicted bandgaps here

should be compared to the fundamental bandgaps[67–70], which are typically larger than the corresponding optical bandgaps due to excitonic effects. Notably, a recent measurement on LCO reports an optical bandgap of about ≈1.3 eV[64].

Regarding magnetic moments, the values obtained by neutron scattering involve uncertainties since the copper form factor is not a priori known. Appendix E of ref. [23] compares copper magnetic moments from various experiments, including the values given in the recent review of Tranquada[7]. Note that, when estimating the copper magnetic moment, we have increased the Wigner–Seitz radius of the integration sphere beyond the default 1.16–1.91 Å (the Cu–O bond length) in order to fully capture the magnetic density centered on the copper atomic site and the part originating from strong hybridization between the copper and oxygen atoms (see Supplementary Discussion 2 in the Supplementary materials for more details).

While these predicted magnetic moments are in approximate agreement with the experimentally measured value, it has been suggested that this is not the correct comparison. This is because (1) given a static magnetic moment, fluctuation can cause a 30% reduction[71]. (2) DFT works with spin symmetry breaking[72], and the DFT magnetic moments should be compared to the static value. We believe this issue is unresolved and that self-consistency can capture some average effects of fluctuation due to the DFT correlation potential. We hope to discuss this further in a future publication.

Figure 6 presents the electronic band dispersions in pristine and doped La_2CuO_4 in the LTO crystal structure for the AFM phase using SCAN, r^{2}SCAN, r^{2}SCAN-L, M06L, and HSE06. The copper (red circles) and planar oxygen (blue dots) orbital contributions are overlayed. For all XC functionals, LCO is seen to be an insulator. At the valence band edge, SCAN, r^{2}SCAN and r^{2}SCAN-L produce a significant avoided crossing between the $d_{x^2-y^2}$ and in-plane oxygen dominated bands along $\Gamma - M$ and $M - \bar{\Gamma}$, but this feature is essentially absent in M06L. In SCAN and r^{2}SCAN, the gap is direct, with its smallest value occurring at M symmetry point or very close to it. In contrast, r^{2}SCAN-L and M06L predict indirect bandgaps. Finally, the conduction bands in M06L display significant spin splittings indicative of ferrimagnetic ordering consistent with the observed ferrimagnetic moments.

Turning to the doped system in Fig. 6, all meta-GGAs are seen to capture the metal-insulator transition, with various XC functionals producing small differences in band splittings around the Fermi level. In contrast, HSE06 maintains a small gap and predicts a nearly flat impurity-like band just above the Fermi level, consistent with the B3LYP results[14]. See Supplementary Figs. 2, 3 and 4 in the Supplementary Materials for further details of the electronic band dispersions in LTO, LTT, and HTT phases. The SCAN-based magnetic moments and bandgaps given in this study differ by ~0.02μ$_B$ and 0.11 eV, respectively, from those given in ref. [22]. These small differences, which do not affect the overall conclusions of ref. [22], are due to an error in the VASP implementation that was used in ref. [22].

Effective U and exchange coupling

The bandgap that develops in the half-filled Cu $d_{x^2-y^2}$ dominated band by splitting the up- and down-spin bands is due to strong multi-orbital intrasite electron–electron interactions. The strength of these interactions is a key quantity that can be used to characterize various regions of the phase diagram and classify the phenomenology of the cuprate family as a whole[73]. In order to estimate the correlation strengths implicit in the underlying XC density functionals, we map our site-resolved partial densities of states to a multi-orbital Hubbard model[74] along the lines of ref. [23]. For this purpose, we consider a d orbital μ of spin σ in a ligand field with on-site correlations in the mean field, and express its

energy as

$$E_\pm^{\mu\sigma} = E_{atomic}^\mu + U\left\langle n_{\mu\bar{\sigma}}^\pm \right\rangle + U' \sum_{\nu\neq\mu}\left\langle n_{\nu\bar{\sigma}}^\pm \right\rangle$$
$$+ (U' - J_H)\sum_{\nu\neq\mu}\left\langle n_{\nu\sigma}^\pm \right\rangle \pm h, \tag{4}$$

where $\pm$ indexes the bonding $(-)$ and anti-bonding $(+)$ states, and h is the hybridization strength. $\mu(\nu)$ and spin $\sigma(\bar{\sigma} = -\sigma)$ are orbital and spin indices, respectively, and $\langle n_{\mu\sigma}^\pm \rangle$ is the average electron occupation for a given state in the mean field. By taking the difference between the up- and down-spin channels and summing over bonding and anti-boding levels, U and J_H can be shown to connect the spin splitting of a given orbital to the differences in various spin-dependent orbital occupations,

$$E^{\mu\uparrow} - E^{\mu\downarrow} = U(N_{\mu\downarrow} - N_{\mu\uparrow}) - J_H\sum_{\nu\neq\mu}(N_{\nu\uparrow} - N_{\nu\downarrow}), \tag{5}$$

where $N_{\mu\sigma} = \sum_\pm \langle n_{\mu\sigma}^\pm \rangle$. Furthermore, $E^{\mu\sigma}$ may be obtained from the density of states:

$$E^{\mu\sigma} = \int_W g_{\mu\sigma}(\varepsilon)\varepsilon d\varepsilon \tag{6}$$

where W represents the bandwidth. The average spin splitting of a given orbital can then be expressed as:

$$E^{\mu\uparrow} - E^{\mu\downarrow} = \int_W [g_{\mu\uparrow}(\varepsilon) - g_{\mu\downarrow}(\varepsilon)]\varepsilon d\varepsilon. \tag{7}$$

We thus arrive at the following coupled set of equations for the interaction parameters,

$$\int_W [g_{\mu\uparrow}(\varepsilon) - g_{\mu\downarrow}(\varepsilon)]\varepsilon d\varepsilon = U(N_{\mu\downarrow} - N_{\mu\uparrow}) - J_H\sum_{\nu\neq\mu}(N_{\nu\uparrow} - N_{\nu\downarrow}). \tag{8}$$

By using the copper-atom-projected partial density-of-states in the AFM phase of LTO La_2CuO_4 where the $d_{x^2-y^2}$ orbital is half-filled and all other orbitals are completely filled, we can simplify the preceding set of coupled equations into the form:

$$\int_W [g_{d_{x^2-y^2}\uparrow}(\varepsilon) - g_{d_{x^2-y^2}\downarrow}(\varepsilon)]\varepsilon d\varepsilon = U/2 \tag{9}$$

$$\int_W [g_{(\mu\neq d_{x^2-y^2})\uparrow}(\varepsilon) - g_{(\mu\neq d_{x^2-y^2})\downarrow}(\varepsilon)]\varepsilon d\varepsilon = J_H/2 \tag{10}$$

Finally, we evaluate $\int_W [g_{\mu\uparrow}(\varepsilon) - g_{\mu\downarrow}(\varepsilon)]\varepsilon d\varepsilon$ over the full band width W for each orbital to solve for U and J_H. The estimated values of U and J_H so obtained are presented in Table 1. The average spin splittings are strongly orbital dependent[23], and we have taken the largest value as the upper bound on J_H.

Results of Table 1 show that TPSS and revTPSS yield a smaller value for U compared to the recent cRPA calculations (~3.2 eV)[75], since they fail to adequately capture the bandgaps and magnetic moments, while M06L, SCAN-L, and r^{2}SCAN-L yield comparable values. MS0, MS2, rSCAN, and r^{2}SCAN, find larger values than the cRPA values. The hybrid HSE06 XC functional predicts exaggerated values for U.

In order to determine the exchange coupling strength, we use a mean-field approach, where we map the total energies of the AFM and ferromagnetic (FM) phases onto those of a nearest-neighbor spin $-\frac{1}{2}$ Heisenberg Hamiltonian[76–78]. The difference in the energies of the AFM and FM phases in the mean-field limit is given by

$$\Delta E = E_{AFM} - E_{FM} = JNZ\langle S \rangle^2 \tag{11}$$

where N is the total number of magnetic sites in the unit cell, $S = 1/2$ is the spin on each site, and Z is the coordination number. Since the in-plane interactions within the Cu–O planes in La_2CuO_4
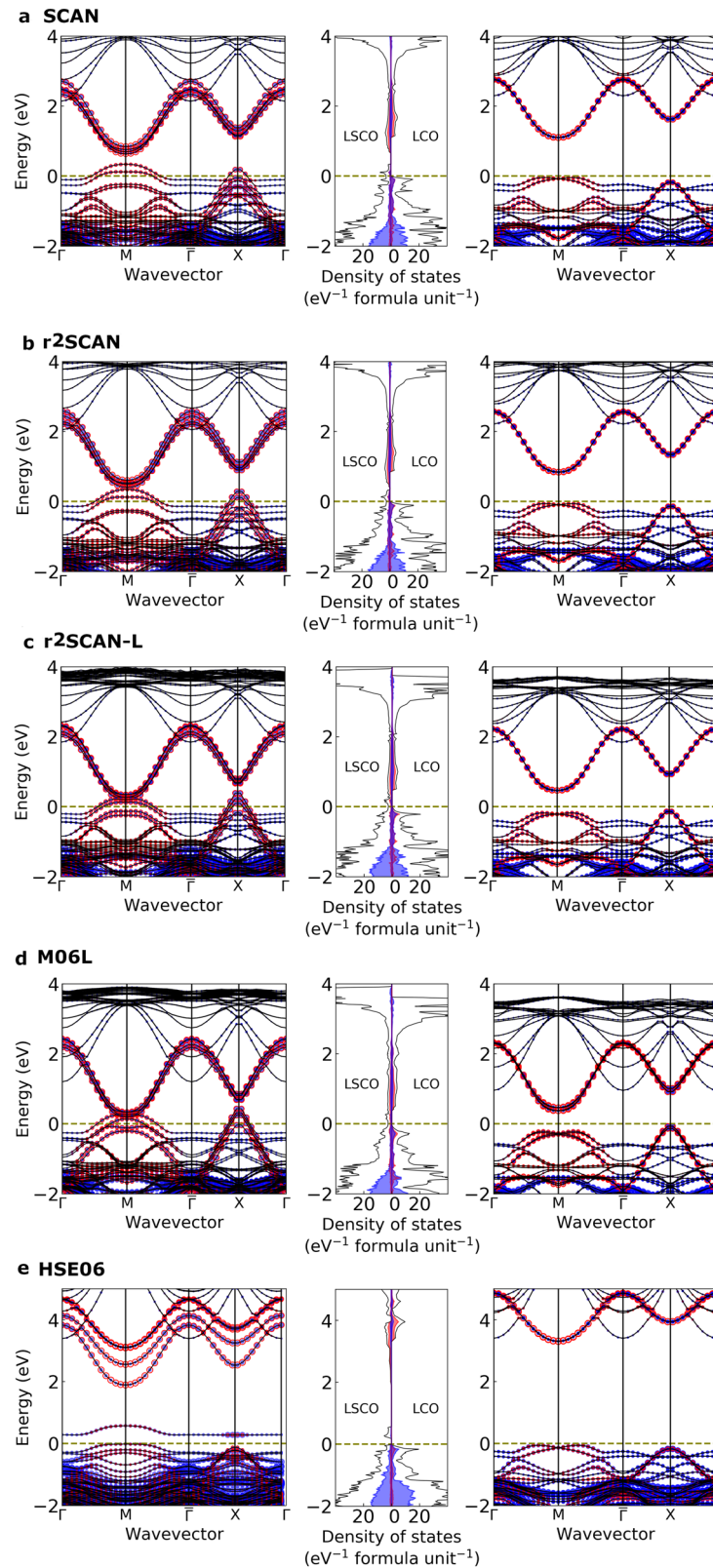
Fig. 6 Band structure and density of states (DOS) from various DFAs. Electronic band structure and density of states of LCO and LSCO in the LTO phase using **a** SCAN, **b** r2SCAN, **c** r2SCAN-L, **d** M06L, **e** HSE06. The contribution of Cu-$d_{x^2-y^2}$ and O-$p_x + p_y$ are marked by the red and blues shadings, respectively. The path followed by the dispersion in the Brillouin zone is shown in Fig. 1b.

Table 1. Theoretically predicted values of U and J_H using various DFAs for three different phases of pristine LCO.

Functional	Phase	U (eV)	J_H (eV)
	LTO	2.23	0.54
TPSS	LTT	2.19	0.55
	HTT	2.19	0.54
	LTO	2.32	0.60
revTPSS	LTT	2.31	0.60
	HTT	2.3	0.58
	LTO	3.14	0.51
M06L	LTT	3.14	0.54
	HTT	3.19	0.55
	LTO	5.60	1.36
MS0	LTT	5.71	1.32
	HTT	5.91	1.34
	LTO	5.00	1.16
MS2	LTT	5.09	1.13
	HTT	5.108	1.18
	LTO	5.40	1.25
SCAN	LTT	5.40	1.27
	HTT	5.36	1.24
	LTO	3.13	0.61
SCAN-L	LTT	3.13	0.61
	HTT	3.16	0.60
	LTO	4.24	1.04
rSCAN	LTT	4.25	1.03
	HTT	4.26	1.02
	LTO	4.45	1.06
r^2SCAN	LTT	4.43	1.06
	HTT	4.41	1.05
	LTO	3.14	0.61
r^2SCAN-L	LTT	3.15	0.62
	HTT	3.16	0.61
	LTO	11.79	1.27
HSE06	LTT	11.30	1.36
	HTT	11.58	1.27

Table 2. Theoretically predicted values of exchange coupling using various XC functionals for three different phases of pristine LCO.

Functional	Phase	J (meV)
	LTO	−26.74
TPSS	LTT	−25.9
	HTT	−22.24
	LTO	−26.89
revTPSS	LTT	−27.47
	HTT	−24.74
M06L	Did not converge	−
	LTO	−158.29
MS0	LTT	−159.36
	HTT	−160.75
	LTO	−140.46
MS2	LTT	−141.76
	HTT	−139.94
	LTO	−131.08
SCAN	LTT	−131.32
	HTT	−125.97
	LTO	−48.48
SCAN-L	LTT	−50.62
	HTT	−49.95
	LTO	−87.16
rSCAN	LTT	−88.37
	HTT	−82.09
	LTO	−93.12
r^2SCAN	LTT	−95.04
	HTT	−88.33
	LTO	−49.01
r^2SCAN-L	LTT	−50.61
	HTT	−49.88
	LTO	−182.11
HSE06	LTT	−188.51
	HTT	−180.27

are much stronger than the interplanar interactions, we take $Z = 4$. For our AFM $\sqrt{2} \times \sqrt{2}$ unit cell, $N = 4$. In this way, we obtain the J values for various XC functionals listed in Table 2.

Table 2 shows that SCAN is most accurate in predicting the experimental value of -133 ± 3 meV[79–81] for the exchange coupling in LCO. MS0 and MS2 slightly overestimate J compared to SCAN. TPSS, revTPSS, SCAN-L, rSCAN, r^2SCAN and r^2SCAN-L underestimate and HSE06 significantly overestimates J. M06L failed to converge for the FM case. Notably, here and in ref. [23], our modeling involves only the nearest-neighbor J in keeping with the related experimental analysis. We would expect some renormalization of the J values if we were to include next and higher nearest neighbors in our modeling.

In order to gain further insight into the multi-orbital nature of the electronic structure, two additional descriptors were estimated: (1) Charge-transfer energies between the Cu 3d and O 2p orbitals (Δ_{dp}); and (2) the tetragonal splitting of the e_g states (Δ_{e_g}), which are defined as

$$\Delta_{dp} = \varepsilon_d - \varepsilon_p \quad (12)$$

and

$$\Delta_{e_g} = \varepsilon_{x^2-y^2} - \varepsilon_{z^2}. \quad (13)$$

The various band centers ε_μ are defined using the corresponding partial density-of-states as

$$\varepsilon_\mu = \frac{\int g_\mu(\varepsilon)\varepsilon d\varepsilon}{\int g_\mu(\varepsilon)d\varepsilon}, \quad (14)$$

along the lines of refs. [82] and [83]. We used an integration window of −8 eV to the top of the band in Eq. (14). This window covers only the anti-bonding bands for Δ_{e_g}. Results of Table 3 show that compared to PBE, the meta-GGAs generally tend to enhance Δ_{dp} and Δ_{e_g} due to the stabilization of the AFM order. TPSS and revTPSS performances are comparable to PBE while other meta-GGAs predict larger Δ_{dp} and Δ_{e_g} values. For the doped case, Δ_{dp} increases, whereas Δ_{e_g} reduces compared to the pristine results. HSE06 predicts significantly large Δ_{dp} and Δ_{e_g} for both pristine and doped cases.

Meta-GGA performance

The present results for the crystal, electronic, and magnetic properties clearly demonstrate that meta-GGAs provide an improvement over LSDA and PBE. Among the various meta-GGAs considered (TPSS, revTPSS, MS0, MS2, SCAN, rSCAN, r^2SCAN,

Table 3. Theoretically predicted values of the charge-transfer energies between Cu $3d$ and O $2p$ orbitals and two Cu energy splitting using various XC functionals for three different phases of pristine LCO and doped LSCO systems.

Functional	Phase	Pristine LCO		Doped LSCO	
		Δ_{dp} (eV)	Δ_{e_g} (eV)	Δ_{dp} (eV)	Δ_{e_g} (eV)
PBE	LTO	2.41	0.74	3.49	0.60
	LTT	2.38	0.75	3.30	0.62
	HTT	2.41	0.79	3.46	0.59
TPSS	LTO	2.41	0.77	3.52	0.62
	LTT	2.23	0.78	3.50	0.63
	HTT	2.26	0.80	3.44	0.63
revTPSS	LTO	2.37	0.77	3.50	0.61
	LTT	2.24	0.78	3.49	0.62
	HTT	2.23	0.80	3.46	0.63
M06L	LTO	2.52	1.00	3.95	0.73
	LTT	2.54	1.06	3.91	0.74
	HTT	2.46	1.07	3.75	0.81
MS0	LTO	2.99	1.34	5.00	1.07
	LTT	2.84	1.37	4.75	1.14
	HTT	2.93	1.35	5.16	1.09
MS2	LTO	3.00	1.21	4.76	0.89
	LTT	2.91	1.22	4.97	0.87
	HTT	2.92	1.20	4.66	0.93
SCAN	LTO	3.01	1.23	4.84	0.95
	LTT	2.93	1.24	4.79	0.95
	HTT	2.92	1.24	4.71	0.96
SCAN-L	LTO	2.64	0.96	4.18	0.72
	LTT	2.54	0.96	4.20	0.72
	HTT	2.49	0.95	3.89	0.80
rSCAN	LTO	2.55	1.06	4.17	0.92
	LTT	2.45	1.08	4.18	0.92
	HTT	2.47	1.12	4.1	0.93
r^{2}SCAN	LTO	2.52	1.08	4.19	0.92
	LTT	2.45	1.09	4.22	0.93
	HTT	2.47	1.13	4.15	0.93
r^{2}SCAN-L	LTO	2.65	0.98	4.18	0.73
	LTT	2.55	0.98	4.21	0.74
	HTT	2.46	0.96	3.91	0.83
HSE06	LTO	7.35	2.76	9.89	2.80
	LTT	6.91	2.82	–	–
	HTT	7.15	2.74	–	–

M06L), M06L is less satisfactory for predicting the LCO properties, which is heavily parameterized for molecular systems. The earlier generalized-KS (gKS) meta-GGAs such as TPSS and revTPSS are less accurate than the more recently developed approximations (e.g., SCAN). The success of SCAN is a consequence of its enforcing all the known 17 rigorous constraints that a semi-local functional can satisfy[21]. In addition, SCAN localizes d electrons better by reducing self-interaction errors that tend to over-delocalize d electrons in the presence of ligands involving s and p electrons[70]. SCAN thus stabilizes the magnetic moment of Cu and opens a sizable bandgap in LCO[22], its shortcomings in exaggerating magnetic moments in $3d$ elemental solids notwithstanding[26].

rSCAN solves the numerical grid issues encountered in SCAN by regularizing the problematic interpolation function of SCAN with a smooth polynomial, which unfortunately violates exact constraints[31,32], and some of rSCAN's transferability is lost[84,85]. r^{2}SCAN retains the smoothness of rSCAN and maximally restores the exact constraints violated by the regularization of rSCAN and it has been shown to improve the accuracy over rSCAN while maintaining the numerical efficiency[32]. In the present study of cuprates, r^{2}SCAN and rSCAN both perform similarly, with only slight underestimations of the bandgaps and magnetic moments.

By replacing the kinetic energy density with the Laplacian of the electron density and thus de-orbitalizing the underlying meta-GGAs, SCAN-L[35] and r^{2}SCAN-L[36] are constructed from SCAN and r^{2}SCAN, respectively. The XC potentials in SCAN-L and r^{2}SCAN-L are locally multiplicative while in their orbital dependent parent functionals, the potentials are non-multiplicative. Perdew et al.[69] have shown that for a given DFA, the gKS orbital bandgap is equal to the corresponding fundamental bandgap in solids, which is defined as the second-order ground-state energy difference with respect to electron number. This indicates that within the gKS formalism a DFA with better total energy also improves the band gap[70]. The preceding statement also applies to DFAs with multiplicative potentials as they have the same potentials in the KS and gKS schemes. The bandgaps and copper magnetic moments from SCAN-L and r^{2}SCAN-L are consistently underestimated compared to the corresponding values from the parent SCAN and r^{2}SCAN XC functionals.

M06L being an empirical functional is heavily parametrized. It is constructed by fitting to molecular data sets, and therefore, it tends to be less reliable for systems outside its fitting set with limited transferability.

Why does HSE06 open a gap in the doped LSCO?

HSE06 with the admixing parameter value of 1/4 works well for bandgap predictions in semiconductors. This improvement is due to the reduction of the self-interaction error present in PBE through the introduction of exact exchange[68,70]. However, Hartree–Fock is not applicable to metallic systems where there is no bandgap to separate the occupied and unoccupied bands. Therefore, hybrid functionals are not suited for metallic systems.

With the preceding consideration in mind, it is reasonable that the HSE06 XC functional produces an insulator in LCO but fails to capture the metal-insulator transition under doping. Figure 7 shows HSE06-based band structures of LSCO for various mixing parameters "a". For $a = 0$, HSE06 is reduced to PBE, and thus predicts LSCO to be metallic. At $a = 0.05$, a slight change in the band structure can be seen: the conduction bands are slightly pushed up and split due to the stabilization of the magnetic moments on Cu, and the bands around the Fermi level at X start to separate from one another. Increasing a to 0.15 results in a separation of the valence bands at the Fermi level and the splitting of the conduction bands, and the two valence bands near the Fermi level split off from the remaining valence bands. Finally, at the standard value of $a = 0.25$, the highest valence band completely splits off, leaving a 0.2 eV gap at the Fermi level. The resulting conduction band displays significant spin splitting, indicative of a strong uncompensated ferrimagnetic order. Our spin-density calculations show that the spin-down band now lies just above the Fermi level where the doped hole is localized in the copper d_{z^2} and apical oxygen p_z hybridized band, see in Supplementary Fig. 5a of the Supplementary Material. Moreover, the band-projected charge density for the spin-down band (Supplementary Fig. 5b) clearly displays a d_{z^2} orbital shape for copper sites and a p_z orbital shape on the apical oxygen sites, similar to the results from B3LYP[14].

The band structures presented in Fig. 7 show that for small values of the mixing parameter (a), the conduction band and valence bands around the M point near the Fermi level are more dominated by copper $d_{x^2-y^2}$ states. As the value of the mixing
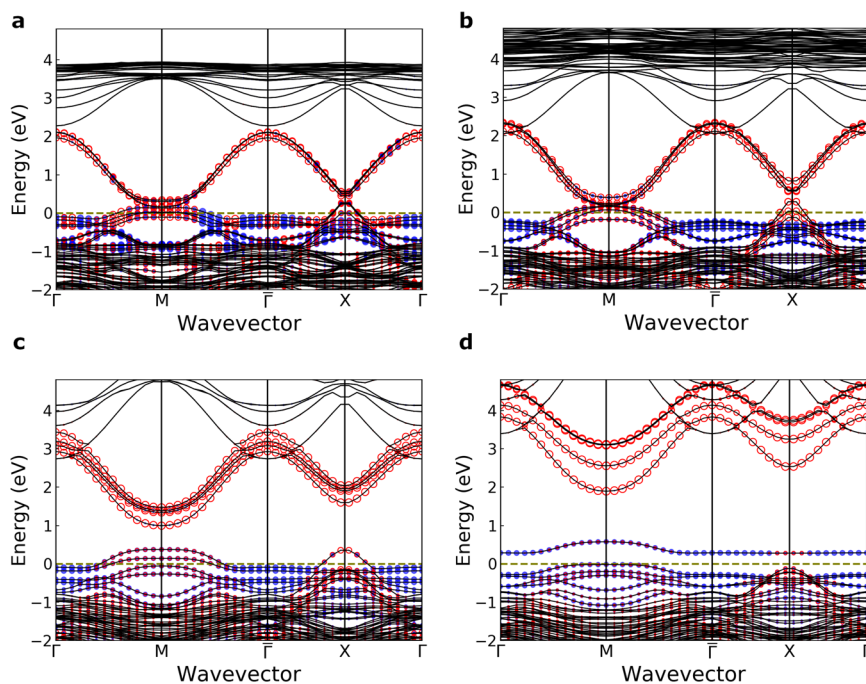
Fig. 7 Band structures for HSE06 functional with different mixing parameter values. Band structure comparison by varying mixing parameter in the HSE06 hybrid functional for **a** $a = 0$, **b** $a = 0.05$, **c** $a = 0.15$, and **d** $a = 0.25$ in doped LTO phase. The blue-filled and red empty circles correspond to copper d_{z^2} and copper $d_{x^2-y^2}$ orbitals, respectively. The projection strength is denoted by marker size.

parameter increases, the copper d_{z^2} orbitals gain more weight. This implies that, as the fraction of exact exchange increases, electrons are more localized on in-plane copper atoms. This is expected since the LSDA gives the extreme covalent regime while the Hartree–Fock leads to the extreme ionicity.

Our study demonstrates that the meta-GGA class of XC functionals within the generalized Kohn–Sham scheme correctly predict many experimental results for pristine LCO, and also capture the insulator-to-metal transition with Sr doping. Among the different meta-GGAs considered, SCAN's performance for structural, electronic, and magnetic properties of LCO/LSCO is closest to the corresponding experimental results. In contrast, the hybrid XC functional (HSE06) fails to capture the metal-insulator transition and overestimates the magnetic moments and band gaps in pristine LCO, and it needs adjustment of the standard 25% value of the mixing parameter to produce the metallic states. Our study thus indicates that the meta-GGAs provide a robust new pathway for the first-principles treatment of strongly correlated materials.

METHODS
Computational methods
The calculations were performed using the pseudopotential projector-augmented wave method[86] implemented in the Vienna ab initio simulation package (VASP)[87,88]. The energy cutoff for the plane-wave basis set was taken to be 550 eV for all meta-GGA calculations and 520 eV for HSE06-based computations. In order to sample the Brillouin zone, for meta-GGAs, an $8 \times 8 \times 4$ Γ-centered k-point mesh was used while a smaller mesh of $6 \times 6 \times 2$ was used for the HSE06 hybrid functional. The structures were initially relaxed for meta-GGAs using a conjugate gradient algorithm with an atomic force tolerance of 0.008 eV/Å and total energy tolerance of 10^{-5} eV. HSE06 calculations on the doped systems were carried out using a damped algorithm. The computational cost for HSE06-based computations is much larger than for the meta-GGAs, and for this reason, a smaller number of k-points and less strict energy tolerance were used in conjunction with using the unrelaxed (experimental) structures.

REFERENCES
1. Bednorz, J. G. & Müller, K. A. Possible high T_c superconductivity in the Ba-La-Cu-O system. *Z. Phys. B Condens. matter* **64**, 189–193 (1986).
2. Hohenberg, P. & Kohn, W. Inhomogeneous electron gas. *Phys. Rev.* **136**, B864 (1964).
3. Kohn, W. & Sham, L. J. Self-consistent equations including exchange and correlation effects. *Phys. Rev.* **140**, A1133 (1965).
4. Pickett, W. E. Electronic structure of the high-temperature oxide superconductors. *Rev. Mod. Phys.* **61**, 433 (1989).
5. Mattheiss, L. Electronic band properties and superconductivity in $La_{2-y}X_yCuO_4$. *Phys. Rev. Lett.* **58**, 1028 (1987).
6. Perdew, J. P. & Zunger, A. Self-interaction correction to density-functional approximations for many-electron systems. *Phys. Rev. B* **23**, 5048 (1981).
7. Tranquada, J. M. *Neutron Scattering Studies of Antiferromagnetic Correlations in Cuprates Handbook of High-Temperature Superconductivity* 257–298 (Springer, Berlin, 2007).
8. Perdew, J. P., Burke, K. & Ernzerhof, M. Generalized gradient approximation made simple. *Phys. Rev. Lett.* **77**, 3865 (1996).
9. Singh, D. & Pickett, W. Gradient-corrected density-functional studies of $CaCuO_2$. *Phys. Rev. B* **44**, 7715 (1991).
10. Becke, A. D. Density-functional exchange-energy approximation with correct asymptotic behavior. *Phys. Rev. A* **38**, 3098 (1988).
11. Lee, C., Yang, W. & Parr, R. G. Development of the Colle-Salvetti correlation-energy formula into a functional of the electron density. *Phys. Rev. B* **37**, 785 (1988).
12. Becke, A. D. A new mixing of Hartree–Fock and local density-functional theories. *J. Chem. Phys.* **98**, 1372–1377 (1993).
13. Stephens, P., Devlin, F., Chabalowski, C. & Frisch, M. J. *Ab initio* calculation of vibrational absorption and circular dichroism spectra using density functional force fields. *J. Phys. Chem.* **98**, 11623–11627 (1994).
14. Perry, J. K., Tahir-Kheli, J. & Goddard III, W. A. *Ab initio* evidence for the formation of impurity $d_{3z^2-r^2}$ holes in doped $La_{2-x}Sr_xCuO_4$. *Phys. Rev. B* **65**, 144501 (2002).

15. Wagner, L. K. & Abbamonte, P. Effect of electron correlation on the electronic structure and spin-lattice coupling of high-T_c cuprates: quantum Monte Carlo calculations. *Phys. Rev. B* **90**, 125129 (2014).

16. Czyżyk, M. & Sawatzky, G. Local-density functional and on-site correlations: the electronic structure of La_2CuO_4 and $LaCuO_3$. *Phys. Rev. B* **49**, 14211 (1994).

17. Pesant, S. & Côté, M. DFT + U study of magnetic order in doped La_2CuO_4 crystals. *Phys. Rev. B* **84**, 085104 (2011).

18. Kotliar, G. et al. Electronic structure calculations with dynamical mean-field theory. *Rev. Mod. Phys.* **78**, 865 (2006).

19. Held, K. et al. Realistic investigations of correlated electron systems with LDA+ DMFT. *Phys. Status Solidi B* **243**, 2599–2631 (2006).

20. Park, H., Haule, K. & Kotliar, G. Cluster dynamical mean field theory of the Mott transition. *Phys. Rev. Lett.* **101**, 186403 (2008).

21. Sun, J., Ruzsinszky, A. & Perdew, J. P. Strongly constrained and appropriately normed semilocal density functional. *Phys. Rev. Lett.* **115**, 036402 (2015).

22. Furness, J. W. et al. An accurate first-principles treatment of doping-dependent electronic structure of high-temperature cuprate superconductors. *Commun. Phys.* **1**, 11 (2018).

23. Lane, C. et al. Antiferromagnetic ground state of La_2CuO_4: a parameter-free abinitio description. *Phys. Rev. B* **98**, 125140 (2018).

24. Zhang, Y. et al. Competing stripe and magnetic phases in the cuprates from first principles. *Proc. Natl Acad. Sci. USA* **117**, 68–72 (2020).

25. Lane, C. et al. First-principles calculation of spin and orbital contributions to magnetically ordered moments in Sr_2IrO_4. *Phys. Rev. B* **101**, 155110 (2020).

26. Isaacs, E. B. & Wolverton, C. Performance of the strongly constrained and appropriately normed density functional for solid-state materials. *Phys. Rev. Mater.* **2**, 063801 (2018).

27. Ekholm, M. et al. Assessing the SCAN functional for itinerant electron ferromagnets. *Phys. Rev. B* **98**, 094413 (2018).

28. Fu, Y. & Singh, D. J. Applicability of the strongly constrained and appropriately normed density functional to transition-metal magnetism. *Phys. Rev. Lett.* **121**, 207201 (2018).

29. Yang, Z.-H., Peng, H., Sun, J. & Perdew, J. P. More realistic band gaps from meta-generalized gradient approximations: only in a generalized Kohn-Sham scheme. *Phys. Rev. B* **93**, 205205 (2016).

30. Furness, J. W. & Sun, J. Enhancing the efficiency of density functionals with an improved iso-orbital indicator. *Phys. Rev. B* **99**, 041119 (2019).

31. Bartók, A. P. & Yates, J. R. Regularized SCAN functional. *J. Chem. Phys.* **150**, 161101 (2019).

32. Furness, J. W., Kaplan, A. D., Ning, J., Perdew, J. P. & Sun, J. Accurate and numerically efficient r²SCAN meta-generalized gradient approximation. *J. Phys. Chem. Lett.* **11**, 8208–8215 (2020).

33. Jones, R. O. & Gunnarsson, O. The density functional formalism, its applications and prospects. *Rev. Mod. Phys.* **61**, 689 (1989).

34. Perdew, J. P. & Wang, Y. Accurate and simple analytic representation of the electron-gas correlation energy. *Phys. Rev. B* **45**, 13244 (1992).

35. Mejia-Rodriguez, D. & Trickey, S. Deorbitalization strategies for meta-generalized-gradient-approximation exchange-correlation functionals. *Phys. Rev. A* **96**, 052512 (2017).

36. Mejía-Rodríguez, D. & Trickey, S. Meta-GGA performance in solids at almost GGA cost. *Phys. Rev. B* **102**, 121109 (2020).

37. Tao, J., Perdew, J. P., Staroverov, V. N. & Scuseria, G. E. Climbing the density functional ladder: nonempirical meta–generalized gradient approximation designed for molecules and solids. *Phys. Rev. Lett.* **91**, 146401 (2003).

38. Perdew, J. P., Ruzsinszky, A., Csonka, G. I., Constantin, L. A. & Sun, J. Workhorse semilocal density functional for condensed matter physics and quantum chemistry. *Phys. Rev. Lett.* **103**, 026403 (2009).

39. Sun, J., Xiao, B. & Ruzsinszky, A. Communication: effect of the orbital-overlap dependence in the meta generalized gradient approximation. *J. Chem. Phys.* **137**, 051101 (2012).

40. Sun, J. et al. Semilocal and hybrid meta-generalized gradient approximations based on the understanding of the kinetic-energy-density dependence. *J. Chem. Phys.* **138**, 044113 (2013).

41. Zhao, Y. & Truhlar, D. G. A new local density functional for main-group thermochemistry, transition metal bonding, thermochemical kinetics, and noncovalent interactions. *J. Chem. Phys.* **125**, 194101 (2006).

42. Heyd, J. Hybrid functionals based on a screened Coulomb potential. *J. Chem. Phys.* **124**, 219906 (2006).

43. Heyd, J., Peralta, J. E., Scuseria, G. E. & Martin, R. L. Energy band gaps and lattice parameters evaluated with the Heyd-Scuseria-Ernzerhof screened hybrid functional. *J. Chem. Phys.* **123**, 174101 (2005).

44. Heyd, J. Efficient hybrid density functional calculations in solids: assessment of the Heyd-Scuseria-Ernzerhof screened Coulomb hybrid functional. *J. Chem. Phys.* **121**, 1187 (2004).

45. Peralta, J. E., Heyd, J., Scuseria, G. E. & Martin, R. L. Spin-orbit splittings and energy band gaps calculated with the Heyd-Scuseria-Ernzerhof screened hybrid functional. *Phys. Rev. B* **74**, 073101 (2006).

46. Perdew, J. P. et al. *Density Functional Theory and its Application to Materials* 1–20 (American Institute of Physics, 2001).

47. Sun, J. et al. Accurate first-principles structures and energies of diversely bonded systems from an efficient density functional. *Nat. Chem.* **8**, 831 (2016).

48. Sun, J. et al. Density functionals that recognize covalent, metallic, and weak bonds. *Phys. Rev. Lett.* **111**, 106401 (2013).

49. Furness, J. W., Kaplan, A. D., Ning, J., Perdew, J. P, & Sun, J. Construction of meta-GGA functionals through restoration of exact constraint adherence to regularized SCAN functionals. *J. Chem. Phys.* **156**, 034109. https://doi.org/10.1063/5.0073623 (2022).

50. Mejia-Rodriguez, D. & Trickey, S. Deorbitalized meta-GGA exchange-correlation functionals in solids. *Phys. Rev. B* **98**, 115161 (2018).

51. Krukau, A. V., Vydrov, O. A., Izmaylov, A. F. & Scuseria, G. E. Influence of the exchange screening parameter on the performance of screened hybrid functionals. *J. Chem. Phys.* **125**, 224106 (2006).

52. Perdew, J. P., Ernzerhof, M. & Burke, K. Rationale for mixing exact exchange with density functional approximations. *J. Chem. Phys.* **105**, 9982–9985 (1996).

53. Vaknin, D. et al. Antiferromagnetism in La_2CuO_{4-y}. *Phys. Rev. Lett.* **58**, 2802 (1987).

54. Freltoft, T., Shirane, G., Mitsuda, S., Remeika, J. & Cooper, A. Magnetic form factor of Cu in La_2CuO_4. *Phys. Rev. B* **37**, 137 (1988).

55. Askerzade, I. *Physical Properties of Unconventional Superconductors Unconventional Superconductors* 1–26 (Springer, 2012).

56. Suter, A. et al. Superconductivity drives magnetism in δ-doped La_2CuO_4. *Phys. Rev. B* **97**, 134522 (2018).

57. Tranquada, J., Sternlieb, B., Axe, J., Nakamura, Y. & Uchida, S. Evidence for stripe correlations of spins and holes in copper oxide superconductors. *Nature* **375**, 561 (1995).

58. Jorgensen, A. J. et al. Superconducting phase of $La_2CuO_{4+\delta}$: a superconducting composition resulting from phase separation. *Phys. Rev. B* **38**, 11337 (1988).

59. Cox, D., Zolliker, P., Axe, J., Moudden, A., Moodenbaugh, A. & Xu, Y. Structural studies of $La_{2-x}Ba_xCuO_4$ between 11–293 K. *Mater Res Soc Symp Proc* **156**, 141–151(1989).

60. Wolf, S. A. & Kresin, V. Z. *Novel Superconductivity* (Springer Science & Business Media, 2012).

61. Zhang, Y., Sun, J., Perdew, J. P. & Wu, X. Comparative first-principles studies of prototypical ferroelectric materials by LDA, GGA, and SCAN meta-GGA. *Phys. Rev. B* **96**, 035143 (2017).

62. Mejía-Rodríguez, D. & Trickey, S. Spin-crossover from a well-behaved, low-cost meta-GGA density functional. *J. Phys. Chem. A* **124**, 9889–9894 (2020).

63. Uchida, S. et al. Optical spectra of $La_{2-x}Sr_xCuO_4$: effect of carrier doping on the electronic structure of the CuO_2 plane. *Phys. Rev. B* **43**, 7942 (1991).

64. Li, Y., Huang, J., Cao, L., Wu, J. & Fei, J. Optical properties of La_2CuO_4 and $La_{2-x}Ca_xCuO_4$ crystallites in UV–vis–NIR region synthesized by sol–gel process. *Mater. Charact.* **64**, 36–42 (2012).

65. Kastner, M., Birgeneau, R., Shirane, G. & Endoh, Y. Magnetic, transport, and optical properties of monolayer copper oxides. *Rev. Mod. Phys.* **70**, 897 (1998).

66. Ono, S., Komiya, S. & Ando, Y. Strong charge fluctuations manifested in the high-temperature Hall coefficient of high-T_c cuprates. *Phys. Rev. B* **75**, 024515 (2007).

67. Cohen, A. J., Mori-Sánchez, P. & Yang, W. Fractional charge perspective on the band gap in density-functional theory. *Phys. Rev. B* **77**, 115123 (2008).

68. Mori-Sánchez, P., Cohen, A. J. & Yang, W. Localization and delocalization errors in density functional theory and implications for band-gap prediction. *Phys. Rev. Lett.* **100**, 146401 (2008).

69. Perdew, J. P. et al. Understanding band gaps of solids in generalized Kohn–Sham theory. *Proc. Natl Acad. Sci. USA* **114**, 2801–2806 (2017).

70. Zhang, Y. et al. Symmetry-breaking polymorphous descriptions for correlated materials without interelectronic U. *Phys. Rev. B* **102**, 045112 (2020).

71. Auerbach, A. *Interacting Electrons and Quantum Magnetism* (Springer Science & Business Media, 2012).

72. Perdew, J. P., Ruzsinszky, A., Sun, J., Nepal, N. K. & Kaplan, A. D. Interpretations of ground-state symmetry breaking and strong correlation in wavefunction and density functional theories. *Proc. Natl Acad. Sci. USA* **118**, e2017850118 (2021).

73. Markiewicz, R., Buda, I., Mistark, P., Lane, C. & Bansil, A. Entropic origin of pseudogap physics and a Mott-Slater transition in cuprates. *Sci. Rep.* **7**, 44008 (2017).

74. Oleś, A. M. Antiferromagnetism and correlation of electrons in transition metals. *Phys. Rev. B* **28**, 327 (1983).

75. Jang, S. W. et al. Direct theoretical evidence for weaker correlations in electron-doped and Hg-based hole-doped cuprates. *Sci. Rep.* **6**, 33397 (2016).

76. Su, Y.-S., Kaplan, T., Mahanti, S. & Harrison, J. Crystal Haartree-Faock calculations for La_2NiO_4 and La_2CuO_4. *Phys. Rev. B* **59**, 10521 (1999).

77. Coffey, D., Bedell, K. & Trugman, S. Effective spin Hamiltonian for the CuO planes in La_2CuO_4 and metamagnetism. *Phys. Rev. B* **42**, 6509 (1990).

78. Noodleman, L. Valence bond description of antiferromagnetic coupling in transition metal dimers. *J. Chem. Phys.* **74**, 5737–5743 (1981).

79. Bourges, P., Casalta, H., Ivanov, A. & Petitgrand, D. Superexchange coupling and spin susceptibility spectral weight in undoped monolayer cuprates. *Phys. Rev. Lett.* **79**, 4906 (1997).

80. Hayden, S. et al. High-energy spin waves in La_2CuO_4. *Phys. Rev. Lett.* **67**, 3622 (1991).

81. Coldea, R. et al. Spin waves and electronic interactions in La_2CuO_4. *Phys. Rev. Lett.* **86**, 5377 (2001).

82. Botana, A. & Norman, M. Similarities and Differences between $LaNiO_2$ and $CaCuO_2$ and implications for superconductivity. *Phys. Rev. X* **10**, 011024 (2020).

83. Jang, S. W., Kotani, T., Kino, H., Kuroki, K. & Han, M. J. Quasiparticle self-consistent GW study of cuprates: electronic structure, model parameters and the two-band theory for T_c. *Sci. Rep.* **5**, 1–10 (2015).

84. Mejía-Rodríguez, D. & Trickey, S. Comment on "Regularized SCAN functional" [J. Chem. Phys. 150, 161101 (2019)]. *J. Chem. Phys.* **151**, 207101 (2019).

85. Bartók, A. P. & Yates, J. R. Response to "Comment on 'Regularized SCAN functional" [J. Chem. Phys. 151, 207101 (2019)]. *J. Chem. Phys.* **151**, 207102 (2019).

86. Kresse, G. & Joubert, D. From ultrasoft pseudopotentials to the projector augmented-wave method. *Phys. Rev. B* **59**, 1758 (1999).

87. Kresse, G. & Furthmüller, J. Efficient iterative schemes for abinitio total-energy calculations using a plane-wave basis set. *Phys. Rev. B* **54**, 11169 (1996).

88. Kresse, G. & Hafner, J. *Ab initio* molecular dynamics for open-shell transition metals. *Phys. Rev. B* **48**, 13115 (1993).

AUTHOR CONTRIBUTIONS

J.S. designed the project. K.P. and J.S. proposed the framework of the computational approach, K.P. performed the calculations. C.L., J.W.F., R.Z., J.N., B.B., R.S.M., Y.Z., A.B., and J.S. analyzed the data and wrote the manuscript.